JWST lensed quasar dark matter survey – I. Description and first results

A. M. Nierenberg [1]⋆†, R. E. Keeley [1], D. Sluse,[2] D. Gilman,[3,4] S. Birrer,[5] T. Treu [6],
K. N. Abazajian [7], T. Anguita [8,9] A. J. Benson [10], V. N. Bennert,[11] S. G. Djorgovski,[12] X. Du,[6]
C. D. Fassnacht,[13] S. F. Hoenig,[14] A. Kusenko,[6,15] C. Lemon [16] M. Malkan,[6] V. Motta,[17]
L. A. Moustakas [18], D. Stern[18] and R. H. Wechsler[19,20,21]

Affiliations are listed at the end of the paper

ABSTRACT

The flux ratios of gravitationally lensed quasars provide a powerful probe of the nature of dark matter. Importantly, these ratios are sensitive to small-scale structure, irrespective of the presence of baryons. This sensitivity may allow us to study the halo mass function even below the scales where galaxies form observable stars. For accurate measurements, it is essential that the quasar's light is emitted from a physical region of the quasar with an angular scale of milliarcseconds or larger; this minimizes microlensing effects by stars within the deflector. The warm dust region of quasars fits this criterion, as it has parsec-size physical scales and dominates the spectral energy distribution of quasars at wavelengths greater than 10 μm. The JWST Mid-Infrared Instrument is adept at detecting redshifted light in this wavelength range, offering both the spatial resolution and sensitivity required for accurate gravitational lensing flux ratio measurements. Here, we introduce our survey designed to measure the warm dust flux ratios of 31 lensed quasars. We discuss the flux-ratio measurement technique and present results for the first target, DES J0405-3308. We find that we can measure the quasar warm dust flux ratios with 3 per cent precision. Our simulations suggest that this precision makes it feasible to detect the presence of 10^7 $M_\odot$ dark matter haloes at cosmological distances. Such haloes are expected to be completely dark in cold dark matter models.

Key words: gravitational lensing: strong – quasars: general – dark matter.

1 INTRODUCTION

Understanding the properties and behaviour of dark matter (DM) is essential to our understanding of structure formation and galaxy formation. Its existence is currently our best model for the structure and evolution of the Universe from scales ranging from the cosmic microwave background (Planck Collaboration 2020) to the rotation curves of spiral galaxies and the dispersion support of spheroidal dwarf galaxies (see, e.g. Weinberg et al. 2015; Bullock & Boylan-Kolchin 2017, and references therein). In this theory, baryonic galaxies form within extended DM haloes (White & Rees 1978; White & Frenk 1991). Direct detection of these dark haloes would provide robust evidence for DM's existence. Moreover, the particle properties of DM, such as its mass, formation mechanism, and possible self-interactions, determine the abundance and internal structure of haloes (see e.g. Buckley & Peter 2018, and references therein). As DM continues to evade laboratory detection and is not guaranteed to be detected directly through non-gravitational interactions, observations of the properties of DM haloes provide a crucial way to test hypotheses about its particle properties.

The 'Cold' DM scenario and cosmological theory, ΛCDM, predicts the existence of dark haloes down to planet masses (Wang

et al. 2020) in many models. Detecting these dark objects, below the expected scale of galaxy formation, would provide strong evidence in support of CDM and rule out entire classes of theories in which these low-mass objects do not exist. For example, warm DM (WDM) refers categorically to scenarios in which free-streaming suppresses the matter power spectrum below a characteristic scale, suppressing the concentration of haloes and precluding their formation below a certain mass scale (Bode, Ostriker & Turok 2001; Schneider et al. 2012; Bose et al. 2016; Ludlow et al. 2016). Self-interacting DM (SIDM) models introduce a self-interaction cross-section between DM particles small enough to preserve the successes of CDM on large scales, but large enough to drive heat conduction through DM haloes. This results in a dynamic evolution of halo density profiles that begins with core formation and eventual core collapse (Spergel & Steinhardt 2000; Balberg, Shapiro & Inagaki 2002; Kaplinghat, Tulin & Yu 2016; Yang & Yu 2021; Zeng et al. 2022; Nadler, Yang & Yu 2023a). Models in which an extremely light boson with a mass $\sim 10^{-22}$eV comprises all or part of the DM, usually referred to as 'ultra-light dark matter' (ULDM) or fuzzy DM, predict suppression of small-scale structure similar to WDM and manifest quantum-mechanical interference effects on galactic scales due to the kpc-scale de Broglie wavelength of the particles (Schive, Chiueh & Broadhurst 2014; Mocz et al. 2017; Chan et al. 2020; Laroche et al. 2022; Powell et al. 2023). More generally, any theory that modifies the linear matter power spectrum on scales $k > 5$ Mpc^{-1} impacts the abundance and internal structure of DM haloes. This includes certain models of

⋆ E-mail: anierenberg@ucmerced.edu
† Brinson Fellow.

inflation, primordial non-Gaussianity, late-decaying DM particles, or a non-zero running spectral index in slow-roll inflation (Zentner & Bullock 2002; Stafford et al. 2020; Ando, Hiroshima & Ishiwata 2022; Gilman et al. 2022; María Ezquiaga, García-Bellido & Vennin 2022; Esteban, Peter & Kim 2023). Primordial black holes (PBHs) are another potential DM candidates that primarily affect the internal structure of subhaloes (Afshordi, McDonald & Spergel 2003; Ricotti, Ostriker & Mack 2008; Carr, Kuhnel & Sandstad 2016; Carr & Kühnel 2020; Dike, Gilman & Treu 2023).

Galaxy-scale strong gravitational lensing can reveal DM structure through its gravitational effects on subgalactic scales, and thus provides insight into its properties (see Vegetti et al. 2023 for a comprehensive review). In a galaxy-scale strong gravitational lens, multiple images of a background source appear due to the deflection of light by a foreground galaxy and its surrounding DM halo. An extended background source, such as a galaxy, will appear warped and distorted by strong lensing, and will often partially encircle the foreground deflector. A more compact source, such as a quasar, typically appears two or four times from the perspective of the observer.[1] The first derivative of the gravitational potential determines the relative positions of the lensed images, while the second derivative of the potential determines their magnifications. Thus, the positions and magnifications of lensed images constrain the mass distribution of the deflector across a range of scales, spanning the size of the Einstein radius (typically ~ 1 arcsec) down to the milliarcsecond scales probed by the image magnifications. These data are therefore sensitive to the abundance and internal structure of DM haloes several orders of magnitude less massive than the main deflector and its host halo. The sensitivity of strong lensing observables to both the abundance and internal structure of haloes has led to constraints on warm DM (Vegetti et al. 2018; Hsueh et al. 2020; Gilman et al. 2020a; Zelko et al. 2022), fuzzy DM (Laroche et al. 2022; Powell et al. 2023), SIDM (Gilman et al. 2021; Minor et al. 2021; Yang & Yu 2021; Nadler, Yang & Yu 2023a), primordial density fluctuations (Gilman et al. 2022), and PBHs (Dike, Gilman & Treu 2023).

The state of the field has evolved considerably since Mao & Schneider (1998) and Dalal & Kochanek (2002) showed that low-mass DM haloes could explain the relative magnifications (or flux ratios) of quadruply imaged radio-loud quasars. In the ensuing decades, the sample of known galaxy-scale strong lenses has grown by an order of magnitude, both through the discovery of new systems and the use of radio-quiet quasars observed at optical and infrared wavelengths. The modelling frameworks used to analyse and interpret data from strong lens systems now include more accurate models for the population of DM haloes perturbing the lenses, including dark haloes along the line of sight (Xu et al. 2012; Despali et al. 2018; Gilman et al. 2019, 2020b; Sengül et al. 2022), correlated structure around the host halo (Gilman et al. 2019), and the tidal evolution of dark subhaloes. The calibration of the substructure models implemented in lensing analyses come from the predictions of numerical simulations of structure formation in early-type galaxies (Fiacconi et al. 2016; Nadler et al. 2023b) and semi-analytic models, including `galacticus` (Benson 2012) and `SatGen` (Jiang et al. 2021). Advances in the modelling of strong lens systems have been enabled by software packages such as `lensmodel`,[2] `lenstronomy`[3] (Birrer & Amara 2018; Birrer et al.

2021), `GLEE` (Suyu & Halkola 2010), `PyAutoLens`[4] (Nightingale et al. 2021), `Herculens`[5] (Galan et al. 2022), and the codes of Vegetti & Koopmans (2009, 2022), which include capabilities to forward-model lensing observables through multiplane lensing computations and simultaneous reconstruction of lensed images and background sources. Finally, open-source packages such as `pyHalo`[6] and `paltas`[7] (Wagner-Carena et al. 2023) interface between lensing codes and DM models to quickly generate populations of DM haloes for lensing simulations.

The background source plays a key role in gravitational lensing inferences of DM structure from image flux ratios because its spatial extent imposes a particular angular and temporal scale on the problem. For substructure lensing studies, the source must be extended enough that the light-crossing time exceeds the arrival time difference between lensed images (typically days to months) so that intrinsic variations in the source produce a negligible change in the flux ratios. For a typical time delay of ~ 10 days, this implies a spatial extent of at least 0.1 pc. The source must also be extended enough to be insensitive to microlensing by stars in the main deflector. The perturbation of an image magnification caused by a halo depends on the deflection angle produced by the halo relative to the angular size of the source (Dobler & Keeton 2006; Metcalf & Amara 2012). Stars produce deflection angles of order $\sim \mu$as. Given typical galaxy-scale lensing configurations, this implies a minimum required source size of $\sim$mas, which corresponds to physical scales of ~ 1 pc at a typical source redshift of $z = 2$. Quasar radio and narrow-line emission are extended enough to meet these criteria (Metcalf & Madau 2001; Moustakas & Metcalf 2003), and these sources have yielded some of the strongest constraints to date on a turnover in the halo mass function (Gilman et al. 2018, 2019; Hsueh et al. 2020), with an upper limit of $M_{hm} < 10^{7.8}$ M$_\odot$ (2σ) (Gilman et al. 2020a). Improvements in this measurement can be made by increasing the sample of lenses, improving the lens modelling techniques applied to interpret the data, improving flux-ratio measurement sensitivity, and choosing sources with intrinsically smaller sizes.

Quasar warm dust serves as an attractive light source for flux-ratio anomaly measurements. This dust component has temperatures of hundreds of Kelvin and dominates the quasar spectral energy distribution at rest-frame wavelengths of $\sim 8-12 \mu$m. It has typical sizes of $\sim 0.1-10$ pc (Burtscher et al. 2013; Leftley et al. 2019), with minimal scaling with quasar luminosity. This is much smaller than the nuclear narrow-line emission with FWHM ~ 100 pc (Müller-Sánchez et al. 2011; Nierenberg et al. 2014, 2017). Fig. 1 demonstrates an example of the magnification induced by a perturbing subhalo on a source with a characteristic size scale of the narrow-line emission compared with the warm dust emission. The size of the quasar warm dust emission region is excellent for DM studies, as it is large enough to be unaffected by microlensing while still being small enough to be significantly magnified by individual low-mass DM haloes. It is also bright and ubiquitous.

Quasar warm dust has long been recognized as a potential source for analyses of DM through strong lensing. Several studies have undertaken IR studies of strongly lensed quasars out to *observed frame* 10 μm (Agol, Jones & Blaes 2000; Chiba et al. 2005; MacLeod, Kochanek & Agol 2009; Ross et al. 2009; Fadely & Keeton 2011; MacLeod et al. 2013; Jones et al. 2019). Chiba et al. (2005) and MacLeod, Kochanek & Agol (2009) both measured flux ratios to be

---

[1] If the source is a quasar surrounded by a galaxy, both extended arcs and multiple images of the quasar appear.

[2] https://www.physics.rutgers.edu/~keeton/gravlens/

[3] https://github.com/lenstronomy/lenstronomy

[4] https://github.com/Jammy2211/PyAutoLens

[5] https://github.com/austinpeel/herculens

[6] https://github.com/dangilman/pyHalo
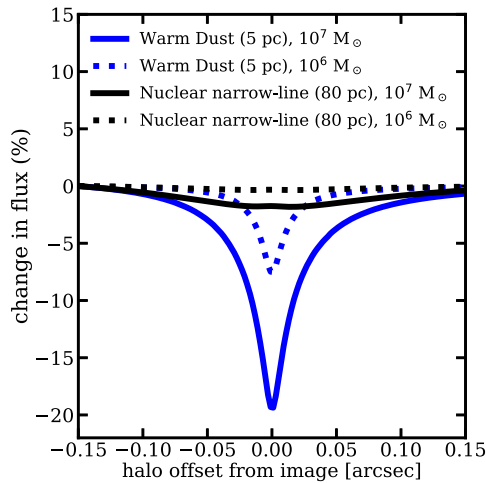
[7] https://github.com/swagnercarena/paltas

Figure 1. Illustration of the differential magnification of a saddle image of a quadruply imaged quasar with a Gaussian light distribution by a perturbing NFW subhalo with masses of 10^6 (dashed lines) and 10^7 M$_\odot$ (solid lines), as a function of the position of the subhalo relative to the centre of the lensed image. Per cent differences in flux are relative to a model without a subhalo. The subhalo significantly alters the flux of the smaller source (blue lines) with FWHM typical of the quasar warm dust region, but it is not massive enough to significantly affect the larger source (black lines) with FWHM typical of the quasar nuclear narrow-line region. The JWST program described in this work aims to have sensitivity to the effects of 10^7 M$_\odot$ subhaloes, which are not expected to contain detectable gas or stars. Our final measurements will be made statistically by generating populations of DM haloes both in the lens and along the line of sight, and by marginalizing over uncertainties in the deflector macromodel and source properties as described in Gilman et al. (2019, 2020a).

consistent with results from lensed radio jets. These studies probed *rest-frame* wavelengths of ∼3–5 μm, where we expect light from the quasar accretion disc as well as both hot and warm dust components (see e.g. Stalevski et al. 2012; Sluse et al. 2013, and references therein). Measuring the flux ratios at even redder wavelengths, where the warm dust dominates the SED, may provide an even more robust constraint of DM structure. This has now become possible with JWST, which has both the spatial resolution and sensitivity to measure lensed quasar flux ratios to *rest frame* 8 μm given typical source redshifts.

Here, we introduce our survey JWST-GO-2056 (PI: Nierenberg) of 31 quadruply lensed quasars in which we use multiband Mid-Infrared Instrument (MIRI) imaging with JWST to measure the warm dust flux ratios. Given typical source sizes of 1–10 pc, and target flux ratio precision of 3 per cent, DM haloes with masses below 10^7 M$_\odot$ can cause a significant perturbation to the flux ratios. No existing data set has demonstrated the capability to reveal the presence of dark haloes on these scales across cosmological distances. Detecting a population of haloes at 10^7M$_\odot$ would have profound consequences for DM physics. Independent confirmation of the presence of dark haloes through lensing would verify a key prediction of the ΛCDM paradigm, complementing other probes of low-mass DM structure, such as studies of dwarf galaxies (e.g. Nadler et al. 2021a; Dekker et al. 2022; Slone et al. 2023) and stellar streams (Bovy, Erkal & Sanders 2017; Banik et al. 2021). Non-detection of these low-mass haloes would falsify CDM, and an inference of their central density profiles and concentrations would improve existing bounds from lensing on SIDM, fuzzy DM, and the matter power spectrum (see Vegetti et al. 2023, and references therein).

This paper is organized as follows. In Section 2, we describe the survey design and sample selection. In Section 3, we present measurements for the first target observed for our program, DES J0405-3308 (Anguita et al. 2018). In Section 4, we describe how we measure the light components. In Section 5, we present our model for fitting the quasar spectral energy distribution. In Section 6, we discuss our results in light of previous measurements of this system. In Section 7, we estimate our sensitivity to DM haloes for the full survey. In Section 8, we provide a summary of the major conclusions of this paper. In order to calculate physical sizes, we assume a flat ΛCDM cosmology with $h = 0.7$ and $\Omega_m = 0.3$.

2 THE QUASAR MID-IR SPECTRAL ENERGY DISTRIBUTION AND SURVEY DESIGN

The goal of this program is to measure the flux ratios of strongly lensed warm dust emission of quasars in order to constrain the properties of DM. Quadruply imaged quasars were selected from the current known sample of ∼50 systems (Inada et al. 2012; Lemon et al. 2017; Agnello et al. 2018; Agnello & Spiniello 2019; Delchambre et al. 2019; Lemon, Auger & McMahon 2019; Stern et al. 2021). These systems were discovered through a combination of data from wide-field surveys including the Sloan Digital Sky Survey (York et al. 2000), the Panoramic Survey Telescope and Rapid Response System (Chambers et al. 2016), *Gaia* (Gaia Collaboration 2023), the *Wide-field Infrared Survey Explorer* (Wright et al. 2010), and the Dark Energy Survey (Dark Energy Survey Collaboration 2016). We first describe the properties of the quasar mid-infrared spectral energy distribution that are relevant to our measurement and explain how this impacted our observation strategy and lens selection. After selecting based on the criteria outlined in the following subsections, the final sample contains 31 lenses. We will provide detailed information for each target in the papers that present flux ratios for those targets.

2.1 Photometric requirements for spectral energy distribution fitting

Our goal is to isolate emission coming from physical regions more extended than ∼0.1 pc in order to ensure that these regions subtend an angular size of ∼mas, and are therefore not contaminated by stellar microlensing in the lens galaxy. This in turn ensures that the flux ratios we measure are sensitive only to the presence of low-mass DM haloes rather than stellar microlensing or intrinsic variability.

The current picture of the mid-IR emitting region of quasars has been built up using a combination of narrow-band imaging, reverberation mapping, and high-resolution interferometric measurements. One model is consistent with all of these observations. In this model, the mid-IR SED of quasars is composed of three relatively distinct sources of emission. At wavelengths below 2 microns, there is significant emission from the quasar accretion disc, which has physical scales of light-days (e.g. Wambsganss, Paczynski & Schneider 1990; Wanders et al. 1997; Anguita et al. 2008; Fausnaugh et al. 2016), corresponding to angular sizes of μas at typical source redshifts. At redder wavelengths, the spectral energy distribution becomes dominated by a 'hot' dust region with peak flux emitted at temperatures ranging from 1000–1400 K (∼3 μm). This emission is associated with dust near the sublimation temperature that marks the inner boundary of the dusty region of the quasar and has characteristic size scales of order 0.05–0.2 pc (Suganuma et al. 2004, 2006; Mor & Trakhtenbrot 2011; GRAVITY Collaboration 2020), depending on quasar luminosity. In addition to this, there is a 'warm' dust component (see e.g. Hönig 2019, and references

therein), which dominates the SED at wavelengths of 8–12 μm. This component is observed to subtend scales of $\sim$0.1–10 pc, with little or no scaling with luminosity (Burtscher et al. 2013; Leftley et al. 2019).

The size of the warm dust makes it both insensitive to microlensing, as well as relatively more sensitive to low mass perturbations than the larger narrow-line region used in previous flux-ratio anomaly studies (Nierenberg et al. 2020; Gilman et al. 2020a). Fig. 1 illustrates this for the case of a saddle image in a quadruply imaged quasar. Saddle images are located at a saddle point in the time-delay surface of the lens and are therefore particularly sensitive to the effects of small-scale perturbations. The smaller source with FWHM of 5 pc, characteristic of the quasar warm dust emitting region, is significantly more perturbed by the subhalo than is the more extended source with FWHM of 80 pc, characteristic of the quasar nuclear narrow-line region. We are aiming for measurements that are sensitive to the presence of individual 10^7 M$_\odot$ NFW haloes.[8] We selected this mass target as it is below the threshold at which the majority of haloes are believed to contain detectable galaxies (e.g. Nadler et al. 2021b). Based on these simulations, we aim for a target flux ratio measurement signal to noise of 3 per cent.

Sluse et al. (2013) performed microlensing analyses of simulated lensed quasars spectral energy distributions and demonstrated that lensed quasar images could be significantly affected by microlensing at rest-frame wavelengths blueward of 8 μm, because of the small physical size of the hot dust emitting region, and the quasar accretion disc. Therefore, ideally, a flux-ratio study of quasars would probe only the warm dust emission at rest-frame wavelengths beyond 10 μm and redder in order to avoid contamination. The reddest MIRI imaging filter is 25.5 μm. Such a restriction on rest-frame wavelength would enable us to study only lensed quasars with redshifts below 1.5.

In order to expand our sample to higher source redshifts, and to ensure a lack of microlensing contamination at lower redshifts, we use multiband imaging spanning the near-to-mid-IR SED of the quasar to constrain the relative contributions of the quasar accretion disc and the hot and warm dust for each lensed image. Based on simulations presented in a companion paper (Sluse et al. in preparation), such multiband imaging enables the identification of lensed images affected by significant microlensing and can be used to reduce systematic uncertainties relative to single-band imaging only.

We adopted the following strategy to measure the spectral energy distribution of lensed quasar images. For all lenses, we obtained imaging in F560W, F1280W, and F1800W to obtain a constraint on the relative brightness of the quasar accretion disc and hot dust emission. We also required the reddest filter to measure rest-frame 6 μm or redder. Thus, for quasars with redshifts $z > 2$, we required the faintest lensed image to be detectable in F2550W. Our target signal-to-noise was 100. Using the pre-launch JWST Exposure Time Calculator, this corresponded to a minimum lensed image flux of 1 mJy. The faintest lensed image fluxes were estimated by applying the optical flux ratios by the unresolved total flux measured in WISE W4 (22.4 μm).

For source quasars with redshifts $z < 2$, F2100W (rest-frame 8 μm or redder) provides sufficiently red wavelength coverage to mitigate microlensing. This filter is much more sensitive than F2550W given the lower background and more compact point-spread function (PSF), and thus we did not impose a minimum flux requirement

for these targets beyond an unresolved detection of the lens in W4 (total W4 flux for all four images greater than $\sim$3 mJy).

Given typical quasar SEDs, and the sensitivity of MIRI imaging as a function of wavelength, these criteria were sufficient to ensure that the quasar flux ratios could be measured with adequate signal-to-noise in the three bluer filters.

In addition to the sensitivity requirements, we selected lenses with a minimum image separation of 0$''$.1 for accurate image deblending, given that the highest resolution imaging is in F560W with a PSF FWHM of 0$''$.2.

2.2 Macromodel requirements

Lenses were selected to have four images to constrain the smooth mass distribution, which is used as a baseline for flux ratio anomaly studies. Furthermore, we required that the lens have a 'simple' deflector light distribution with no significant disc, and only a single massive deflector was needed to reproduce the observed image positions.

3 OBSERVATIONS AND INITIAL REDUCTION

The first system to be observed was DESJ040559.7-330851.00 (Anguita et al. 2018). This lens has source redshift of $z_s = 1.713$ and a photometrically estimated deflector redshift of $z_d \sim 0.3$ (Gilman et al. 2020a). DESJ0405-3308 has an unresolved W4 flux of 7.7 mJy. Assuming the optical flux ratios are identical to the F2550W flux ratios, this would indicate an expected faint image flux of approximately 1.3 mJy. Based on our photometric criteria, this was bright enough to use F2550W as the reddest filter for this target, enabling us to measure fluxes at rest frame $\sim$9.4 μm, where we expect little to no contamination from microlensing. For this system, the spectral energy distribution will provide a useful test of our SED fitting method.

Observations for DESJ0405-3308 were obtained on 2022 October 27. Exposure times were 58 s in F560W, F1280W, and F1800W and 574 s in F2550W. All exposures were divided into a three-point dither pattern to improve spatial resolution and mitigate cosmic rays.

Initial calibration was performed using the default JWST data calibration pipeline[9] (Greenfield & Miller 2016; Bushouse et al. 2022). Sky subtraction of Level 2 data products was performed using customized routines[10] before drizzling to produce the final images. The final pixel scale was set to 0$''$.11 per pixel, identical to the native detector pixel scale. Reduced images in each filter are shown in Figs 2–5.[11]

4 IMAGE FLUX MEASUREMENT

Our goal was to accurately measure the lensed image fluxes in the presence of other light components including the lensed quasar host galaxy (which appears as a lensed arc) and the deflector galaxy light.

---

[8]In CDM, we expect large numbers of such subhaloes and therefore we will model their collective effects.

[9]Using the `jwst_1041.pmap` context file.

[10]Based on https://github.com/STScI-MIRI/Imaging_ExampleNB

[11]The MIRI imager sensitivity at long wavelengths appears to have dropped over the first 6 months of its operation: https://www.stsci.edu/contents/news/jwst/2023/miri-imager-reduced-count-rate?Type = miri. If we simply assume that the time history of this sensitivity drop was similar to what has been more definitively measured for MIRI spectroscopy at $\lambda \geq 20\,\mu$m – https://jwst-docs.stsci.edu/jwst-calibration-pipeline-caveats/jwst-miri-mrs-pipeline-caveats, this would imply that the 2550W fluxes we measure are underestimated by about 10 per cent.
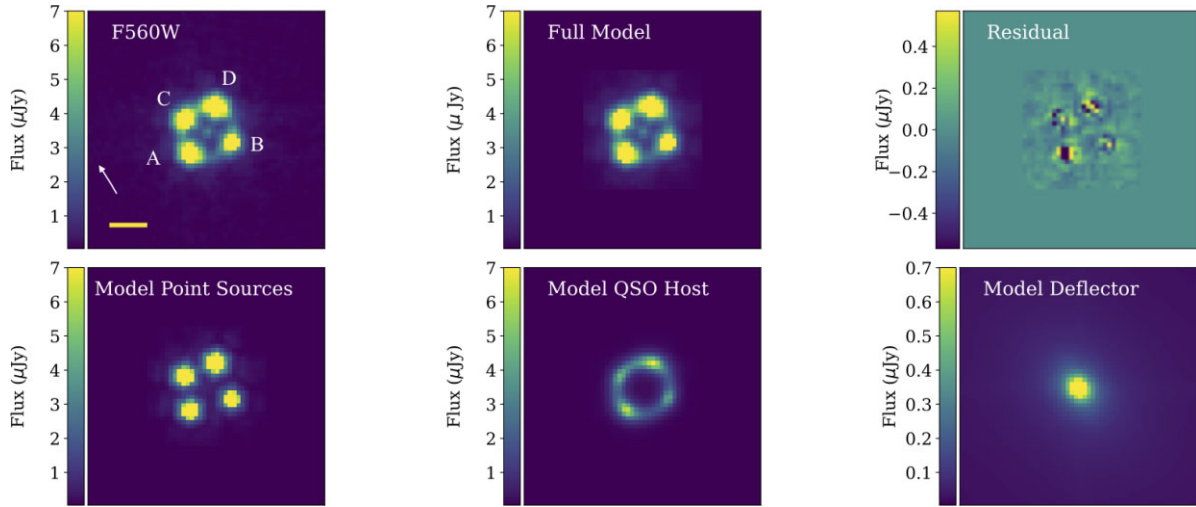
Figure 2. Upper panels: From left to right: Comparison of original F560W image, best-fitting model, and residuals. Lower panels: Separate light model components. From left to right: model point sources, lensed quasar host galaxy, and deflector light distribution. The yellow bar in the lower left of the data image indicates 1 arcsec. The arrow indicates North.
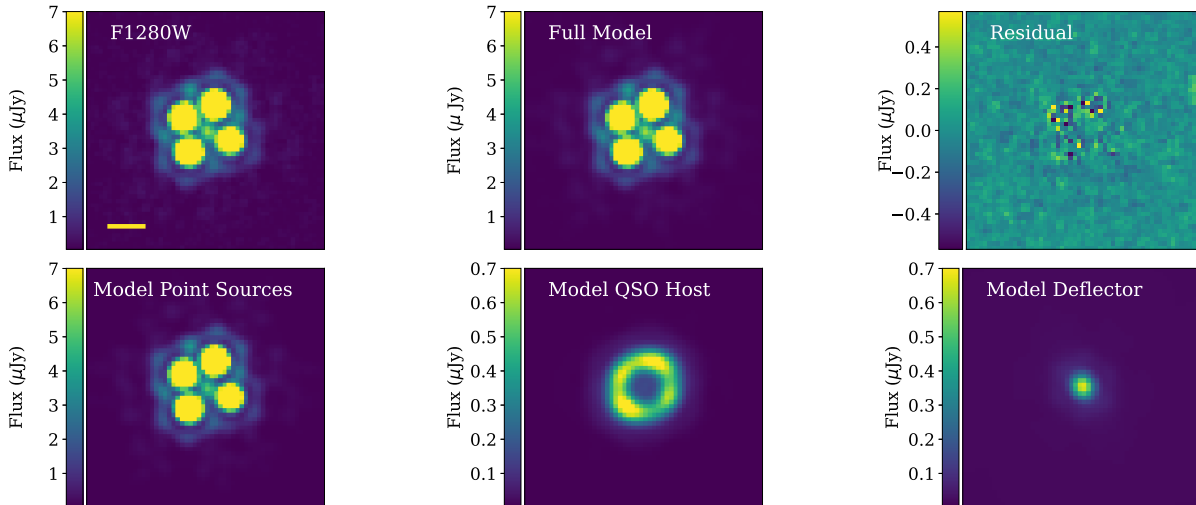

Figure 3. Upper panels: From left to right: Comparison of original F1280W image, best-fitting model, and residuals. Lower panels: Separate light model components. From left to right: model point sources, lensed quasar host galaxy, and deflector light distribution. The yellow bar in the lower left of the data image indicates 1 arcsec.

We adopted a forward modelling approach to measure the lensed quasar image fluxes in all four filters. The model consisted of a combination of up to four light components depending on the filter, as described below.

Lensed quasar images: The quasar light is dominated by the accretion disc and hot and warm dust on angular size scales of micro- to milliarcseconds. Given that this is smaller than the smallest imaging PSF with FWHM of F560W of 0″.2, we treated these components as point sources. We wished our measurement to have as little dependence as possible on the gravitational lensing model, as the image fluxes will later be used to constrain this model with DM substructure. Therefore, we did not associate the point source fluxes or positions with a lens model but rather treated them as completely independent. This is the same procedure one might adopt if, for example, there were foreground stars in the data.

Deflector light distribution: The lens galaxy is detected in F560W and F1280W. We modelled this light distribution as an elliptical Sérsic profile (Sérsic 1963).

Lensed quasar host galaxy: The lensed host galaxy of the quasar is apparent as an extended arc in F560W, F1280W, and F1800W. We modelled the unlensed quasar host galaxy light distribution as an elliptical Sérsic profile. To produce the observed gravitationally lensed arc, we included a gravitational lensing model for the deflector mass distribution. We adopted an elliptical power-law model (Tessore & Metcalf 2015), with external shear.

4.1 PSF fitting

We used webbPSF[12] (Perrin et al. 2012, 2014) to fit the PSF in our data. We used a supersampling of three in order to enable improved astrometric precision, and because of the large detector pixel scale relative to the sizes of the light features such as the lensed quasar host galaxy. At the time of writing, this software was in
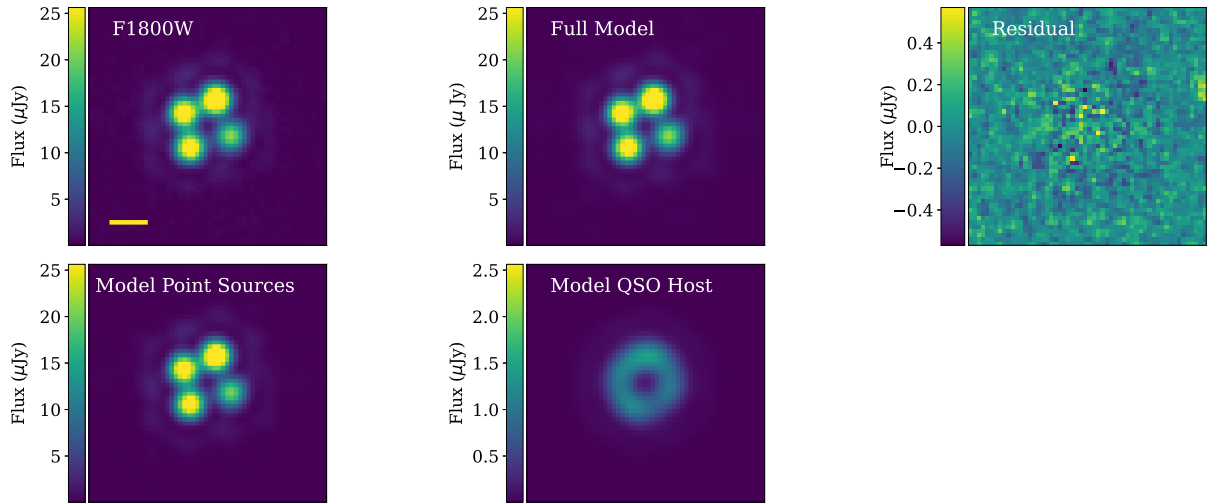
---

[12]Development branch 1.2.1.

Figure 4. Upper panels: From left to right: Comparison of original F1800W image, best-fitting model, and residuals. Lower panels: Separate light model components. From left to right: Model point sources and lensed quasar host galaxy. The deflector light is not detected in this filter, thus it is not included in the model. The yellow bar in the lower left of the data image indicates 1 arcsec.
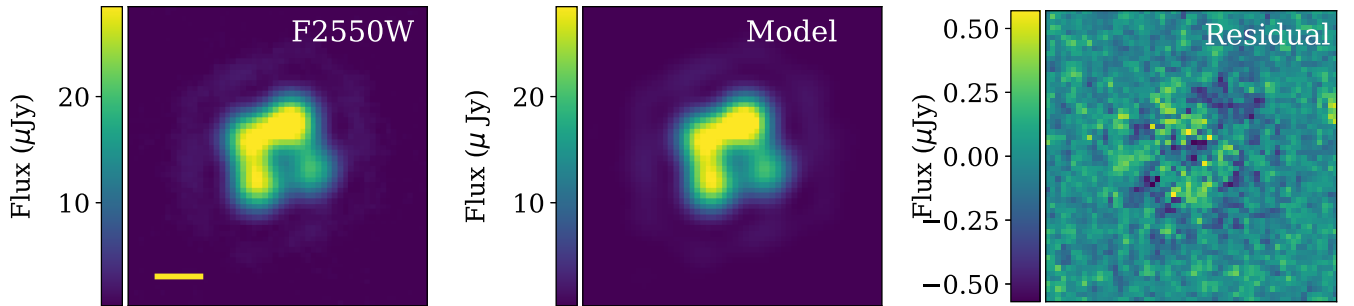

Figure 5. From left to right: Comparison of original image, model, and residuals. The light model in F2550W consists of only the point source contribution. The yellow bar in the lower left of the data image indicates 1 arcsec.

active development to update the models to match observed optics and detector properties. The default parameters provided a poor fit to the observed data due to detector-level effects. The dominant discrepancy was due to inter-pixel capacitance and charge diffusion in the detector (e.g. Argyriou et al. 2023). A preliminary model for the charge diffusion effect has been implemented. However, at the time of writing, this was only in the detector-sampled PSF models, while we required a super-sampled PSF model given the large pixel size relative to the light features.

As an alternative, we found that the PSF could be modelled by varying the `webbPSF` Gaussian 'jitter_sigma' parameter. The 'jitter' effect is implemented in `webbPSF` by convolving the PSF model with a Gaussian kernel to account for spacecraft motion. In practice, the jitter effect has a nearly equivalent impact on the data, as does charge diffusion.[13] The jitter_sigma value was optimized for each filter as described in the following.

We used blackbodies at the redshift of the quasar to account for the wavelength dependence of the PSF. The temperature of each blackbody was optimized separately for each filter. Although in principle the PSF spectrum should be connected to the SED of the quasar (rather than a single blackbody), we found that a single blackbody model for the PSF source provided an excellent fit to

the data. We defer incorporating additional complexity in the PSF simulation until the PSF model has been further refined based on in-flight results.

In addition to the charge diffusion effects, F560W displays a prominent 'cruciform' artefact (Gáspár et al. 2021; Wright et al. 2023), which is a wavelength-dependent, detector-level artefact apparent beyond the first Airy ring. The second extension output of `webbPSF` provides a model for this feature that provides an improved fit relative to the PSF model without it. However, residuals owing to the cross artefact were still prominent in our data. We therefore fit the F560W data in a relatively small region where the cross feature was sub-dominant.

4.2 Modelling procedure

We adopted an iterative approach to fitting our images, switching between optimizing the PSF parameters (jitter_sigma and blackbody temperature), and the parameters associated with light sources and gravitational lensing model until both inferences were returning stable results. Due to the small number of stars in the field of view, and their very different SED from our quasar images, we fit the PSF parameters directly using our lensed quasar images.

We fit the three images that contain the lensed quasar host galaxy simultaneously. We required the image positions, gravitational lens model, and the centroids of the deflector and source light to be the

---

[13]M. Perrin, private communication.

Table 1. Best-fitting `webbPSFjitter_sigma` and blackbody temperature for each filter. These values were inferred for our data using `webbPSF` development version 1.2.1, and do not include inter-pixel capacitance effects.

Parameter	F560W	F1280W	F1800W	F2550W
`jitter_sigma`	$0''.063$	$0''.061$	$0''.073$	$0''.075$
Temperature (K)	1120	700	680	250

Table 2. Measured image positions and fluxes in units of mJy. Image positions are measured from the F2550W data. Image naming follows Shajib et al. (2019), and image labels are shown in Fig. 3. We estimate the flux ratio (absolute flux) uncertainties to be 6 (15), 2 (15), 2 (15), 1 per cent (20 per cent) in F560W, F1280W, F1800W, and F2550W, respectively. The right ascension and declination offsets of the quasar images with respect to image B are within $0''.007$ of those measured by Nierenberg et al. (2020).

Image	dRa	dDec	F560W	F1280W	F1800W	F2550W
A	1.065	0.318	0.396	1.06	1.38	2.647
B	0	0	0.279	0.656	0.875	1.787
C	0.721	1.152	0.459	1.08	1.42	2.790
D	−0.153	1.018	0.536	1.34	1.73	3.357

same between the three filters but allowed all other model parameters to vary between the three filters. F2550W, which contained only four point sources, was fit independently with no lens model and only the four independent PSFs.

After finding the best-fitting model parameters, uncertainties were estimated using a Markov Chain Monte Carlo with the PSF held fixed at the best-fitting value obtained from the previous steps. Given that the flux ratios show no variation over a broad range of PSF model parameters (including those that provide a poor overall fit to the data), we do not anticipate that this choice will make a significant impact on the estimate of the flux-ratio uncertainties. We used `lenstronomy` (Birrer, Amara & Refregier 2015; Birrer & Amara 2018; Birrer et al. 2021) for all image fitting and simulation.

4.3 Results of forward modelling and uncertainty estimation

The best-fitting PSF parameters are given in Table 1, and the measured image fluxes and positions are given in Table 2. Fig. 6 shows the measured flux ratios as a function of wavelength.

We do not report the lens model parameters. Owing to the limitations of the current PSF model as well as the fact that the quasar images are treated as independent foreground objects, the lens and light model parameters we infer cannot be meaningfully compared to other studies for this system, which were based on *Hubble Space Telescope* data with a well-modelled PSF (Shajib et al. 2019; Schmidt et al. 2023). Ultimately, for our gravitational lensing DM measurement, we will apply the approach used by Gilman et al. (2019, 2020a) in which only the image positions and flux ratios are used to constrain the mass distribution of the deflector. This allows for a high degree of flexibility in the smooth mass distribution used as the baseline for the flux-ratio comparison (see also Nierenberg et al. 2020). Below we discuss our tests for the dependence of measurement uncertainty on model choices.

The formal statistical uncertainties for the image fluxes, positions, and flux ratios were extremely small. Here we describe how we estimated systematic uncertainties due to model choices. When estimating uncertainties, it is important to make the distinction between *absolute fluxes*, which are relevant to SED fitting described in
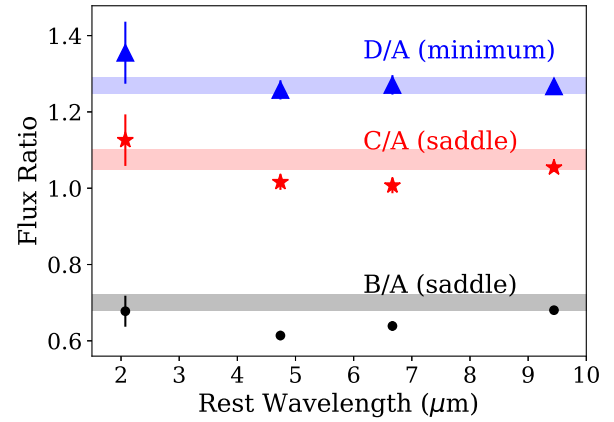
Figure 6. The measured flux ratios with respect to image A as a function of rest-frame wavelength. Coloured bands indicate the 68 per cent confidence interval of the corresponding warm dust component, which is not expected to be microlensed. The labels indicate whether the image is located at a minimum or saddle point of the time delay surface. Image A is a minimum. Rest wavelengths blueward of 8 μm rest frame have significant contributions from the hot dust and accretion disc that are small enough to be microlensed by stars in the lens galaxy and/or time variable on the day-to-week time-scales.

Section 5, and *flux ratios*, which are the key quantity for gravitational lensing estimates.

Position uncertainties: We estimate the systematic uncertainties by comparing the measured relative image positions with those measured in HST WFC3-IR F140W direct imaging from Nierenberg et al. (2020), and find maximum relative offsets of $0''.007$ in the lensed image positions. This is much smaller than the pixel sizes of $0''.11$ for JWST MIRI and $0''.13$ for HST WFC3-IR.

Light component modelling: We performed several tests of the systematic uncertainties on measured image fluxes and flux ratios. These included: (1) Fitting the light in the imaging bands together and requiring the model light components to have the same parameters except amplitude in all three bands; (2) performing the fits in the three filters separately and allowing the lens model to be different in each filter; 3) restricting the source light to be round in shape; 4) restricting the host mass profile to have a slope of $\gamma_p = 2$ rather than allowing it to vary freely; and 5) fixing the image positions to those specified by the lens model, rather than treating them as completely independent foreground light sources. As an additional test on the flux ratios, we measured the flux ratios before and after including the lensed quasar host galaxy.

The extended source was most significant in F560W, contributing approximately 40 per cent of the flux at the location of the quasar images. In F1280W and F1800W the flux was less than 10 per cent at the location of the quasar images. This is reflected in the systematic uncertainties from the tests above, in which we found that the absolute fluxes varied by 5 per cent in F560W and F1280W and 2 per cent in F1800W, and the flux ratios varied by up to 6 per cent in F560W and 1 per cent in F1280W and F1800W.

PSF uncertainties: We found that variations in the choice of PSF model impacted the *absolute* image fluxes by 10 per cent or less. We also tested for variation of PSF within a filter as a function of image brightness. Therefore we did an additional fit of the F2550W data, allowing each point source to have a different `jitter_sigma` value. We found no significant variation in the value of this parameter between the four images, indicating that the adoption of a single PSF model was sufficient for this system. Furthermore, even with the

variable PSF, the flux ratios and fluxes varied by less than 1 per cent relative to a fit in which the PSF was the same for all four images.

Instrument calibration: The absolute flux calibration uncertainties for MIRI have not been estimated at the time of writing. In August 2023, a significant wavelength-dependent loss in sensitivity of 3 per cent for F1280W, 8 per cent for F1800W, and 18 per cent for F2550W was reported for the MIRI imager relative to the commissioning sensitivity measured in Summer 2022.[14] The sensitivity loss seems to have occurred over time. At the time of writing it is not known what the sensitivity loss was at the time of the observations for this program (October 2022), therefore we include the August 2023 reported loss values as an additional systematic uncertainty in our absolute flux measurements.

Conclusion of uncertainty estimate testing: Based on our tests of systematic sources of uncertainty, we find that the absolute flux uncertainty is likely dominated by the uncertainty in the instrument calibration. For this work, we adopt 15 per cent flux uncertainties in F560W, F1280W, and F1800W, and 20 per cent flux uncertainties in F2550W based on our current knowledge of the detector calibration. We expect these uncertainties to become smaller in the near future as the instrument behaviour is better understood.

The dominant source of flux ratio uncertainty in F560W was 6 per cent from modelling the lensed quasar host galaxy, while the uncertainties related to PSF modelling and lensed quasar host galaxy modelling were comparable for the flux ratio measurements in F1280W and F1800W. We adopt flux ratio uncertainties for 2 per cent in these filters. For F2550W, which did not have an apparent lensed quasar host galaxy, we estimate 1 per cent flux ratio uncertainties.

5 SED FITTING

In this section, we describe how we used the MIRI four-band photometry to fit the multicomponent SED and isolate light coming from the warm dust region of the quasar, which is extended enough to avoid contamination from microlensing as described in Section 2.

We followed Sluse et al. (2013) and adopted a simple three-component model of the quasar spectral energy distribution. This is composed of power-law continuum emission from the quasar accretion disc combined with two blackbodies representing the hot dust component, with prior temperature range of 500–1800 K, and the warm dust component, with prior temperature range 100–500 K. We did not include emission lines such as PAH emission, which we expect to make a small contribution to the broad-band fluxes (e.g. García-Bernete et al. 2022).

Our SED model allowed for independent variation of each component amplitude for each lensed image to account for the fact that both the quasar accretion disc and the hot dust are small enough to be affected by microlensing. This also accounts for intrinsic flux variation of the accretion disc on time-scales shorter than the time delay between the lensed images (of order days) (Schmidt et al. 2023). We performed the SED fit simultaneously for all four images. The temperatures of the hot and warm dust blackbodies were allowed to vary as free parameters but were restricted to be the same for all images. The overall SED amplitudes were also allowed to vary independently to account for different overall magnifications for the lensed images.

When fitting the lensed quasar SEDs, we computed the joint likelihood that each set of model parameters would reproduce the

observed *flux ratios* (B/A, C/A, and D/A) in each filter as well as the likelihood that the model matched the *absolute fluxes* for image A in each filter. Model SEDs were transformed into band fluxes following Gordon et al. (2022).[15] We used `emcee` (Foreman-Mackey et al. 2013) to estimate the posterior probability distribution.

Fig. 7 shows the accepted model drawn from the Markov Chain Monte Carlo, while inferred component flux ratios for the hot and warm dust blackbodies are presented in Table 3. The flux ratios are computed by dividing the normalization of the blackbody component for a given image by the normalization of the corresponding blackbody component for image A. Although we included the continuum emission in our model to estimate the uncertainty it might contribute, we do not present the continuum flux ratios as its contribution to the fluxes was small (<10 per cent) in the observed band-passes.

6 DISCUSSION

Here we discuss the results of SED fitting and flux ratio measurements in light of other studies of this system.

6.1 SED fitting results

The hot dust temperature was inferred to be 1200 ± 100 K, and the warm dust temperature was 300 ± 100 K. Interestingly, these values are consistent with the best-fit `webbPSF` blackbody temperature parameters for F560W (1130 K) and F2550W (250 K, Table 1). In these filters, the SED model predicts the flux is dominated by the hot and warm dust components respectively.

The hot dust flux ratios are significantly different from the warm dust flux ratios for images B and C. This is reflected in the flux ratios displayed in Fig. 2, which are nearly achromatic for D/A but show small chromatic changes for B and C. A microlensing explanation would be consistent with results from Nierenberg et al. (2020), who found clear signatures of microlensing in image C, which had a wider H β emission line in C band relative to the other three images. Deformation of the broad emission line profile (such as H β) is a noted signature of microlensing (e.g. Sluse et al. 2012; Fian et al. 2021), and reflects the differential lensing by stars of the higher velocity wings emitted from the smaller parts of the broad-line region.

From the SED fitting, we see that the flux from the warm dust is dominant relative to the hot dust. This is consistent with typical quasar SEDs which find a lower covering fraction of hot dust relative to warm dust (Mor & Trakhtenbrot 2011). From this result, we expect little contamination in F2550W from the more compact hot dust region. We find that the warm dust flux ratios for this system are consistent with the F2550W flux ratios.

6.2 Comparison with past results

There is a significant difference between the cold dust flux ratios and the [O III] flux ratios for image C measured by Nierenberg et al. (2020). As discussed in the Introduction, the [O III] and warm dust emission regions are both extended and not subject to microlensing or time-variability on the day-to-month time-scales relevant to galaxy-scale lenses. Therefore, the differences in flux ratios cannot be explained by these phenomena. Furthermore, differential dust extinction is not a likely explanation as the [O III] emission is redshifted to ~1 μm at the redshift of the deflector, and the quasar warm

---

[14]https://www.stsci.edu/contents/news/jwst/2023/miri-imager-reduced-count-rate?page=1&keyword = MIRI

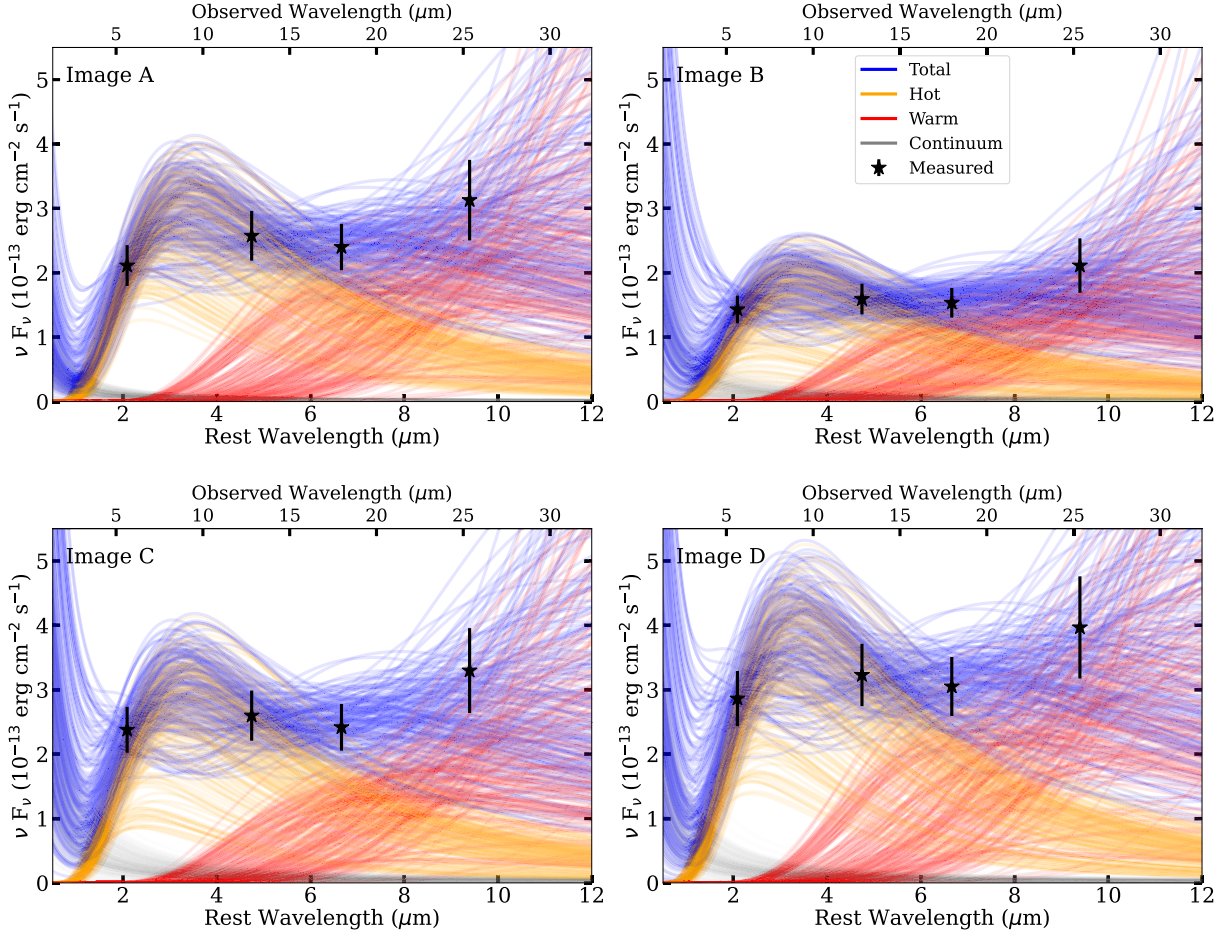[15]https://github.com/STScI-MIRI/ImagingFluxCal/blob/main/model_fluxes.py

Figure 7. Results for SED fitting for separate lensed quasar images fit to a model with continuum plus hot and warm blackbody components with variable temperature. These components represent the quasar accretion disc (grey) and the hot (orange) and warm dust (red) contributions, respectively. The amplitude of each model component varied freely between images to accommodate size-dependent microlensing, intrinsic variability, and lensing by the main deflector and potential DM substructure. The fits are required to reproduce the observed absolute fluxes as well as the flux ratios in each filter. See Section 5 for a description of the model. Each line represents an accepted Markov Chain Monte Carlo draw to illustrate the variations in models.

Table 3. Flux ratios and 1σ uncertainties measured through SED fitting, F2550W, and narrow-line [O III] from Nierenberg et al. (2020).

Ratio	Hot	Warm	F2550W	[O III]
B/A	$0.58^{+0.04}_{-0.07}$	0.70 ± 0.02	0.7 ± 0.007	0.65 ± 0.04
C/A	$0.96^{+0.04}_{-0.07}$	$1.07^{+0.03}_{-0.02}$	1.05 ± 0.01	1.25 ± 0.03
D/A	$1.23^{+0.04}_{-0.06}$	1.27 ± 0.02	1.27 ± 0.01	1.17 ± 0.04

torus light is redshifted well beyond this. Assuming all measurement uncertainties have been accurately characterized, we explore two possible explanations below.

An offset between the centroid of the [O III] emission and the warm torus emission could create a small difference in the flux ratios. Offsets have been observed to be of order tens of parsecs (Singha et al. 2022) between the nuclear narrow-line region and the quasar accretion disc. We tested the impact such an offset would make by choosing a macro model that fits the measured image positions and flux ratios, and offsetting the source from the best-fit position. A 10 pc offset, for example, would create a flux-ratio difference of up to 2 per cent and change the image positions by up to 0.″007. However, the flux-ratio changes are not independent of each other and there is no source offset that reproduces both

the image positions and flux ratios for the [O III] and warm dust in this system. Further investigation of the grism data from Nierenberg et al. (2020) with simulated offsets between the continuum and the [O III] region on the two-dimensional grism data would enable limits to be placed on the possible magnitude of such an offset for this system.

Another explanation for the difference in flux ratios is differential millilensing by low mass perturbers. The mid-IR and [O III] sources have intrinsically different characteristic sizes. The two sources could be magnified differently by the same mass perturber. A qualitative example of this effect is provided in Fig. 1, in which a small source like the warm torus is strongly de-magnified by a perturbing subhalo, while a larger narrow-line region source is not. As with the example lensed image in Fig. 1, image C is a saddle image and we would therefore typically expect it to be de-magnified by a local perturbation to the macromodel, thus the observed in the flux ratios could be explained by this type of phenomenon. The differential effect of such a perturbation on the narrow and warm dust flux-ratios would depend on a variety of factors including both the mass of the perturbation and the intrinsic size of the narrow-line region. Based on the grism spectra, Nierenberg et al. (2020) placed an approximate upper limit of ~100 pc on the FWHM of the narrow-line region for this system based on a lack of differential extension

in the spectra of the four lensed images. Such a differential extension would be observed in the grism spectrum if the narrow-line emission was partially resolved (see also Nierenberg et al. 2017). As a test, we started with a macromodel that fits the observed [O III] flux ratios and image positions. Assuming the [O III] emitting region has an FWHM of 50 pc, a perturbation with mass scale 10^7 M$_\odot$ could reproduce the observed warm torus flux ratios for this system while leaving the [O III] flux ratios unchanged.

In reality, we expect many low-mass haloes in the lens and along the line of sight, potentially perturbing all four images simultaneously, therefore we defer a more meaningful physical interpretation of the discrepancy between the [O III] flux ratios and the mid-IR flux ratios until we have included the effects of full populations of haloes and subhaloes (Keeley et al. in preparation).

7 DM CONSTRAINTS FORECAST

Given the flux-ratio precision measured in this work, we can estimate the constraint on DM properties obtainable from the full sample based on the scaling simulations by Gilman et al. (2019). The current WDM constraint is based on a sample of eight lenses with approximately 6 per cent measurement precision. Extrapolating to 31 lenses with a 3 per cent measurement precision for the relative flux ratios yields an estimated 95 per cent upper limit on a turnover in the half-mode mass M_{hm} of below 10^7 M$_\odot$ if DM is cold. This would correspond to a limit on a thermal relic particle mass above 9.7 keV. The current limit from lensing is $M_{hm} < 10^{7.8}$ ($M_{WDM} > 5.2$ keV) based on eight lenses with narrow-line measurements (Gilman et al. 2020a). Constraining the half-mode mass to be below 10^7 M$_\odot$ would imply the existence of completely dark subhaloes and provide a validation of a major prediction of CDM.

In addition to WDM, Gilman et al. (2021) showed that the compact sources in the JWST data set make these data highly sensitive to the internal structure of haloes. This has particularly relevant consequences for SIDM, which can cause haloes to undergo core collapse, raising their central densities and therefore their lensing efficiency. Based on the forecasts by Gilman et al. (2021) and the analysis with existing data performed by Gilman, Zhong & Bovy (2023), the sample size of lenses obtained through this JWST program should enable constraints on self-interaction cross-sections in which > 40 per cent of haloes core collapse. The properties of the SIDM cross-section required to produce this quantity of collapsed objects depend on the degree to which tidal stripping and evaporation alter the collapse times for subhaloes and on the nature of the self-interaction itself. Keeley et al. (2023) demonstrated that this data set will enable the detection of a mixture of DM made of 50 per cent WDM with half-mode mass of $10^{8.5}$ M$_\odot$ and 50 per cent CDM. Similarly, major improvements will be obtained for limits on all DM models that produce observed consequences on these scales, including, for example, fuzzy DM and PBHs.

8 SUMMARY

We present flux-ratio measurements for DES J0405-3308, the first of 31 systems to be observed in our program to measure rest-frame mid-IR flux ratios of quadruply imaged quasars with JWST.

Our main conclusions are as follows:

(i) We find that the MIRI PSF is well fit when significant additional jitter is added to the model, and when the source spectrum is treated as a blackbody with variable temperature in each filter.

(ii) The flux ratios can be measured to an estimated 6, 2, 2, and 1 per cent precision in F560W, F1280W, F1800W, and F2550W, respectively, with the dominant source of uncertainty coming from modelling the lensed quasar host galaxy light in the three bluer filters and from the PSF in F2550W. The absolute flux uncertainties are estimated to be dominated by ongoing instrument calibrations. For this work, we adopt 15 per cent uncertainties in F560W, F1280W, and F1800W, and 20 per cent in F2550W, but we expect these to improve in the future.

(iii) We introduce an SED-fitting method that enables us to take into account the high flux-ratio precision and the relatively uncertain absolute flux precision. This model fits for the temperatures of the dust components as well as the relative amplitudes of each component in each lensed image.

(iv) We estimate the hot and cold dust temperatures for the source to be 1200 ± 100 K and 300 ± 100 K. The hot dust region shows substantial microlensing relative to the warm dust region, confirming the subparsec size of this region.

(v) The flux ratios inferred from the warm dust component of SED fitting are consistent with the flux ratios measured in F2550W. Given current absolute and flux-ratio measurement uncertainties, the warm dust emission flux ratios can be measured to 3 per cent with 1σ uncertainty. This sensitivity will enable us to infer population-level statistics of DM haloes below masses of 10^7 M$_\odot$ in future work, thus providing a test of a key prediction of CDM.

(vi) The F2550W and warm dust flux ratios are inconsistent at a 20 per cent level with narrow-line flux ratios measured by Nierenberg et al. (2020). This can potentially be explained by the presence of a low-mass DM halo magnifying the smaller warm torus light, but not significantly affecting the more extended narrow-line region image fluxes. Full modelling of the substructure and finite size effects, to be presented in a future paper, will be used to study the origin of the discrepancy in more detail.

DATA AVAILABILITY

The data underlying this article are subject to a proprietary period of 1 yr from the observation date, 2022 October 27. Once the proprietary period expires, the data will be available from the Barbara A. Mikulski Archive for Space Telescopes. The data may also be shared before this time upon reasonable request to the corresponding author.

REFERENCES

Afshordi N., McDonald P., Spergel D. N., 2003, ApJ, 594, L71
Agnello A., Spiniello C., 2019, MNRAS, 489, 2525
Agnello A. et al., 2018, MNRAS, 479, 4345
Agol E., Jones B., Blaes O., 2000, ApJ, 545, 657
Ando S., Hiroshima N., Ishiwata K., 2022, Phys. Rev. D, 106, 103014
Anguita T., Schmidt R. W., Turner E. L., Wambsganss J., Webster R. L., Loomis K. A., Long D., McMillan R., 2008, A&A, 480, 327
Anguita T. et al., 2018, MNRAS, 480, 5017
Argyriou I. et al., 2023, A&A, 680, A96
Balberg S., Shapiro S. L., Inagaki S., 2002, ApJ, 568, 475
Banik N., Bovy J., Bertone G., Erkal D., de Boer T. J. L., 2021, MNRAS, 502, 2364
Benson A. J., 2012, 17, 175
Birrer S., Amara A., 2018, Phys. Dark Universe, 22, 189
Birrer S., Amara A., Refregier A., 2015, ApJ, 813, 102
Birrer S. et al., 2021, J. Open Source Softw., 6, 3283
Bode P., Ostriker J. P., Turok N., 2001, ApJ, 556, 93
Bose S., Hellwing W. A., Frenk C. S., Jenkins A., Lovell M. R., Helly J. C., Li B., 2016, MNRAS, 455, 318
Bovy J., Erkal D., Sanders J. L., 2017, MNRAS, 466, 628
Buckley M. R., Peter A. H. G., 2018, Phys. Rep., 761, 1
Bullock J. S., Boylan-Kolchin M., 2017, ARA&A, 55, 343
Burtscher L. et al., 2013, A&A, 558, A149
Bushouse H. et al., 2022, JWST Calibration Pipeline (1.8.2), Zenodo, https://doi.org/10.5281/zenodo.7229890
Carr B., Kühnel F., 2020, Annu. Rev. Nucl. Part. Sci., 70, 355
Carr B., Kuhnel F., Sandstad M., 2016, Phys. Rev. D, 94, 083504
Chambers K. C. et al., 2016, The Pan-STARRS1 Surveys, https://ui.adsabs.harvard.edu/abs/2016arXiv161205560C
Chan J. H. H., Schive H.-Y., Wong S.-K., Chiueh T., Broadhurst T., 2020, Phys. Rev. Lett., 125, 111102
Chiba M., Minezaki T., Kashikawa N., Kataza H., Inoue K. T., 2005, ApJ, 627, 53
Dalal N., Kochanek C. S., 2002, ApJ, 572, 25
Dark Energy Survey Collaboration, 2016, MNRAS, 460, 1270
Dekker A., Ando S., Correa C. A., Ng K. C. Y., 2022, Phys. Rev. D, 106, 123026
Delchambre L. et al., 2019, A&A, 622, A165
Despali G., Vegetti S., White S. D. M., Giocoli C., van den Bosch F. C., 2018, MNRAS, 475, 5424
Dike V., Gilman D., Treu T., 2023, MNRAS, 522, 5434
Dobler G., Keeton C. R., 2006, MNRAS, 365, 1243
Esteban I., Peter A. H. G., Kim S. Y., 2023, preprint (arXiv:2306.04674)
Fadely R., Keeton C. R., 2011, AJ, 141, 101
Fausnaugh M. M. et al., 2016, ApJ, 821, 56
Fiacconi D., Madau P., Potter D., Stadel J., 2016, ApJ, 824, 144
Fian C., Mediavilla E., Motta V., Jiménez-Vicente J., Muñoz J. A., Chelouche D., Hanslmeier A., 2021, A&A, 653, A109
Foreman-Mackey D., Hogg D. W., Lang D., Goodman J., 2013, PASP, 125, 306
GRAVITY Collaboration, 2020, A&A, 634, A1
Gaia Collaboration, 2023, A&A, 674, A1
Galan A., Peel A., Vernardos G., Biggio L., Courbin F., Starck J.-L., 2022, Astrophysics Source Code Library, record ascl:2209.002
García-Bernete I. et al., 2022, A&A, 666, L5
Gilman D., Birrer S., Treu T., Keeton C. R., Nierenberg A., 2018, MNRAS, 481, 819
Gilman D., Birrer S., Treu T., Nierenberg A., Benson A., 2019, MNRAS, 487, 5721
Gilman D., Birrer S., Nierenberg A., Treu T., Du X., Benson A., 2020a, MNRAS, 491, 6077
Gilman D., Du X., Benson A., Birrer S., Nierenberg A., Treu T., 2020b, MNRAS, 492, L12
Gilman D., Bovy J., Treu T., Nierenberg A., Birrer S., Benson A., Sameie O., 2021, MNRAS, 507, 2432
Gilman D., Benson A., Bovy J., Birrer S., Treu T., Nierenberg A., 2022, MNRAS, 512, 3163
Gilman D., Zhong Y.-M., Bovy J., 2023, Phys. Rev. D, 107, 103008
Gordon K. D. et al., 2022, AJ, 163, 267
Greenfield P., Miller T., 2016, Astron. Comput., 16, 41
Gáspár A. et al., 2021, PASP, 133, 014504
Hsueh J. W., Enzi W., Vegetti S., Auger M. W., Fassnacht C. D., Despali G., Koopmans L. V. E., McKean J. P., 2020, MNRAS, 492, 3047
Hönig S. F., 2019, ApJ, 884, 171
Inada N. et al., 2012, AJ, 143, 119
Jiang F., Dekel A., Freundlich J., van den Bosch F. C., Green S. B., Hopkins P. F., Benson A., Du X., 2021, MNRAS, 502, 621
Jones T. J., Williams L. L. R., Ertel S., Hinz P. M., Vaz A., Walsh S., Webster R., 2019, AJ, 158, 237
Kaplinghat M., Tulin S., Yu H.-B., 2016, Phys. Rev. Lett., 116, 041302
Keeley R. E., Nierenberg A. M., Gilman D., Birrer S., Benson A., Treu T., 2023, MNRAS
Laroche A., Gilman D., Li X., Bovy J., Du X., 2022, MNRAS, 517, 1867
Leftley J. H., Hönig S. F., Asmus D., Tristram K. R. W., Gandhi P., Kishimoto M., Venanzi M., Williamson D. J., 2019, ApJ, 886, 55
Lemon C. A., Auger M. W., McMahon R. G., Koposov S. E., 2017, MNRAS, 472, 5023
Lemon C. A., Auger M. W., McMahon R. G., 2019, MNRAS, 483, 4242
Ludlow A. D., Bose S., Angulo R. E., Wang L., Hellwing W. A., Navarro J. F., Cole S., Frenk C. S., 2016, MNRAS, 460, 1214
MacLeod C. L., Kochanek C. S., Agol E., 2009, ApJ, 699, 1578
MacLeod C. L., Jones R., Agol E., Kochanek C. S., 2013, ApJ, 773, 35
Mao S., Schneider P., 1998, MNRAS, 295, 587
María Ezquiaga J., García-Bellido J., Vennin V., 2022, preprint (arXiv:2207.06317)
Metcalf R. B., Amara A., 2012, MNRAS, 419, 3414
Metcalf R. B., Madau P., 2001, ApJ, 563, 9
Minor Q., Gad-Nasr S., Kaplinghat M., Vegetti S., 2021, MNRAS, 507, 1662
Mocz P., Vogelsberger M., Robles V. H., Zavala J., Boylan-Kolchin M., Fialkov A., Hernquist L., 2017, MNRAS, 471, 4559
Mor R., Trakhtenbrot B., 2011, ApJ, 737, L36
Moustakas L. A., Metcalf R. B., 2003, MNRAS, 339, 607
Müller-Sánchez F., Prieto M. A., Hicks E. K. S., Vives-Arias H., Davies R. I., Malkan M., Tacconi L. J., Genzel R., 2011, ApJ, 739, 69
Nadler E. O. et al., 2021a, Phys. Rev. Lett., 126, 091101

Nadler E. O., Birrer S., Gilman D., Wechsler R. H., Du X., Benson A., Nierenberg A. M., Treu T., 2021b, ApJ, 917, 7

Nadler E. O., Yang D., Yu H.-B., 2023a, ApJL, 958, L39

Nadler E. O. et al., 2023b, ApJ, 945, 159

Nierenberg A. M., Treu T., Wright S. A., Fassnacht C. D., Auger M. W., 2014, MNRAS, 442, 2434

Nierenberg A. M. et al., 2017, MNRAS, 471, 2224

Nierenberg A. M. et al., 2020, MNRAS, 492, 5314

Nightingale J. et al., 2021, J. Open Source Softw., 6, 2825

Perrin M. D., Soummer R., Elliott E. M., Lallo M. D., Sivaramakrishnan A., 2012, in Space Telescopes and Instrumentation 2012: Optical, Infrared, and Millimeter Wave. SPIE, p. 1193, https://www.spiedigitallibrary.org/conference-proceedings-of-spie/8442/84423D/Simulating-point-spread-functions-for-the-James-Webb-Space-Telescope/10.1117/12.925230.full

Perrin M. D., Sivaramakrishnan A., Lajoie C.-P., Elliott E., Pueyo L., Ravindranath S., Albert L., 2014, in Space Telescopes and Instrumentation 2014: Optical, Infrared, and Millimeter Wave. SPIE, p. 1174, https://www.spiedigitallibrary.org/conference-proceedings-of-spie/9143/91433X/Updated-point-spread-function-simulations-for-JWST-with-WebbPSF/10.1117/12.2056689.full

Planck Collaboration, 2020, A&A, 641, A6

Powell D. M., Vegetti S., McKean J. P., White S. D. M., Ferreira E. G. M., May S., Spingola C., 2023, MNRAS, 524, L84

Ricotti M., Ostriker J. P., Mack K. J., 2008, ApJ, 680, 829

Ross N. R., Assef R. J., Kochanek C. S., Falco E., Poindexter S. D., 2009, ApJ, 702, 472

Schive H.-Y., Chiueh T., Broadhurst T., 2014, Nat. Phys., 10, 496

Schmidt T. et al., 2023, MNRAS, 518, 1260

Schneider A., Smith R. E., Macciò A. V., Moore B., 2012, MNRAS, 424, 684

Sengül A. Ç., Dvorkin C., Ostdiek B., Tsang A., 2022, MNRAS, 515, 4391

Shajib A. J. et al., 2019, MNRAS, 483, 5649

Singha M. et al., 2022, A&A, 659, A123

Slone O., Jiang F., Lisanti M., Kaplinghat M., 2023, Phys. Rev. D, 107, 043014

Sluse D., Hutsemékers D., Courbin F., Meylan G., Wambsganss J., 2012, A&A, 544, A62

Sluse D., Kishimoto M., Anguita T., Wucknitz O., Wambsganss J., 2013, A&A, 553, A53

Spergel D. N., Steinhardt P. J., 2000, Phys. Rev. Lett., 84, 3760

Stafford S. G., McCarthy I. G., Crain R. A., Salcido J., Schaye J., Font A. S., Kwan J., Pfeifer S., 2020, MNRAS, 493, 676

Stalevski M., Jovanović P., Popović L. Č., Baes M., 2012, MNRAS, 425, 1576

Stern D. et al., 2021, ApJ, 921, 42

Suganuma M. et al., 2004, ApJ, 612, L113

Suganuma M. et al., 2006, ApJ, 639, 46

Suyu S. H., Halkola A., 2010, A&A, 524, A94

Sérsic J. L., 1963, Boletin de la Asociacion Argentina de Astronomia La Plata Argentina, 6, 41

Tessore N., Metcalf R. B., 2015, A&A, 580, A79

Vegetti S., Koopmans L. V. E., 2009, MNRAS, 392, 945

Vegetti S., Despali G., Lovell M. R., Enzi W., 2018, MNRAS, 481, 3661

Vegetti S. et al., 2023, preprint (arXiv:2306.11781)

Vernardos G., Koopmans L. V. E., 2022, MNRAS, 516, 1347

Wagner-Carena S., Aalbers J., Birrer S., Nadler E. O., Darragh-Ford E., Marshall P. J., Wechsler R. H., 2023, ApJ, 942, 75

Wambsganss J., Paczynski B., Schneider P., 1990, ApJ, 358, L33

Wanders I. et al., 1997, ApJS, 113, 69

Wang J., Bose S., Frenk C. S., Gao L., Jenkins A., Springel V., White S. D. M., 2020, Nature, 585, 39

Weinberg D. H., Bullock J. S., Governato F., Kuzio de Naray R., Peter A. H. G., 2015, Proc. Natl. Acad. Sci. USA, 112, 12249

White S. D. M., Frenk C. S., 1991, ApJ, 379, 52

White S. D. M., Rees M. J., 1978, MNRAS, 183, 341

Wright E. L. et al., 2010, AJ, 140, 1868

Wright G. S. et al., 2023, PASP, 135, 048003

Xu D. D., Mao S., Cooper A. P., Gao L., Frenk C. S., Angulo R. E., Helly J., 2012, MNRAS, 421, 2553

Yang D., Yu H.-B., 2021, Phys. Rev. D, 104, 103031

York D. G. et al., 2000, AJ, 120, 1579

Zelko I. A., Treu T., Abazajian K. N., Gilman D., Benson A. J., Birrer S., Nierenberg A. M., Kusenko A., 2022, Phys. Rev. Lett., 129, 191301

Zeng Z. C., Peter A. H. G., Du X., Benson A., Kim S., Jiang F., Cyr-Racine F.-Y., Vogelsberger M., 2022, MNRAS, 513, 4845

Zentner A. R., Bullock J. S., 2002, Phys. Rev. D, 66, 043003

[1]*University of California, Merced, 5200 N Lake Road, Merced, CA 95341, USA*

[2]*STAR Institute, Quartier Agora – Allé du six Août, 19c, B-4000 Liège, Belgium*

[3]*Department of Astronomy & Astrophysics, University of Chicago, Chicago, IL 60637, USA*

[4]*Department of Astronomy and Astrophysics, University of Toronto, 50 St. George Street, Toronto, ON M5S 3H4, Canada*

[5]*Department of Physics and Astronomy, Stony Brook University, Stony Brook, NY 11794, USA*

[6]*UCLA Physics & Astronomy, 475 Portola Plaza, Los Angeles, CA 90095-1547, USA*

[7]*Department of Physics and Astronomy, University of California, Irvine, CA 92697-4575, USA*

[8]*Instituto de Astrofisica, Departamento de Ciencias Fisicas, Universidad Andres Bello, Santiago, 7550196, Chile*

[9]*Millennium Institute of Astrophysics, Santiago, 7500011, Chile*

[10]*Carnegie Institution for Science, Pasadena, CA 91101, USA*

[11]*Physics Department, California Polytechnic State University, San Luis Obispo, CA 93407, USA*

[12]*California Institute of Technology, Pasadena, CA 91125, USA*

[13]*Department of Physics and Astronomy, UC Davis, 1 Shields Ave., Davis, CA 95616, USA*

[14]*School of Physics and Astronomy, University of Southampton, Southampton SO17 1BJ, UK*

[15]*Kavli Institute for the Physics and Mathematics of the Universe (WPI), UTIAS, The University of Tokyo, Kashiwa, Chiba 277-8583, Japan*

[16]*Institute of Physics, Laboratory of Astrophysics, Ecole Polytechnique Fédérale de Lausanne (EPFL), Observatoire de Sauverny, CH-1290 Versoix, Switzerland*

[17]*Instituto de Física y Astronomía, Universidad de Valparaíso, Avda. Gran Bretaña 1111, Valparaíso, 2340000, Chile*

[18]*Jet Propulsion Laboratory, California Institute of Technology, 4800 Oak Grove Dr, Pasadena, CA 91109, USA*

[19]*Kavli Institute for Particle Astrophysics & Cosmology, P.O. Box 2450, Stanford University, Stanford, CA 94305, USA*

[20]*Department of Physics, Stanford University, 382 Via Pueblo Mall, Stanford, CA 94305, USA*

[21]*SLAC National Accelerator Laboratory, Menlo Park, CA 94025, USA*

This paper has been typeset from a TEX/LATEX file prepared by the author.